

## Three-dimensional flow structures of turbulence in precessing spheroids

Ken Komoda and Susumu Goto\*

*Graduate School of Engineering Science, Osaka University, 1-3 Machikaneyama,  
Toyonaka, Osaka 560-8531, Japan*



(Received 4 July 2018; published 22 January 2019)

We conduct direct numerical simulations of turbulence sustained in slowly precessing spheroids with the absolute value of the ellipticity  $\eta$  being between zero (i.e., a sphere) and 0.2. Using a flexible grid generation algorithm, we can effectively simulate flows in an arbitrarily shaped container. This enables us to investigate the ellipticity dependence of the precession-driven flow in spheroids with the spin and precession axes being at a right angle. The numerical results are in excellent agreement with experimental data under the same flow conditions. In particular, we numerically realize hysteresis loops, which have been well known since the seminal experiments by Malkus [Science **160**, 259 (1968)], connecting two qualitatively different states in a precessing spheroid with non-negligible ellipticity  $|\eta|$  larger than about  $10/\sqrt{\text{Re}}$  (where  $\text{Re}$  denotes the Reynolds number defined by using the spin angular velocity). Our numerical simulations reveal the three-dimensional turbulent flow structures in these states. One is a high-energy state where the mean flow is approximated by a uniform-vorticity flow. The other is a low-energy state with twisted mean-flow streamlines, which lead to fully developed turbulence when the Reynolds number is high enough. The mean-flow structures in the low-energy state are common irrespective of the ellipticity; namely, the main component of the mean flow is a circulation about the axis perpendicular both to the spin and precession axes, but the torsion of the mean-flow streamlines is larger for smaller  $\eta$ . For sufficiently high Reynolds numbers, the low-energy state and therefore developed turbulence are sustained for the Poincaré number (the precession rate) larger than about  $|\eta|/2$ . On the other hand, stronger precession leads to the significant reduction of turbulence in a central region of the container. Hence, a container with smaller  $|\eta|$  is adequate to sustain developed turbulence with weak precession.

DOI: [10.1103/PhysRevFluids.4.014603](https://doi.org/10.1103/PhysRevFluids.4.014603)

### I. INTRODUCTION

We investigate the flow of an incompressible fluid confined in a rotating container whose spin axis precesses about another axis perpendicular to itself (Fig. 1). The most remarkable feature of the precession-driven flow is that, despite the simple container motion, the sustained flow states and their dependence on the parameters (the spin and precession rates) are highly nontrivial. In particular, a weak precession can drive strong turbulence. This feature has been attracting geophysicists because it is an important issue whether or not the weak precession of the Earth affects the geodynamo. The turbulence sustained without stirrers in a smooth cavity is attractive also in engineering applications, and it is an interesting scientific unsolved problem to reveal the origin of the strong turbulence driven by weak precession of a container.

---

\*goto@me.es.osaka-u.ac.jp

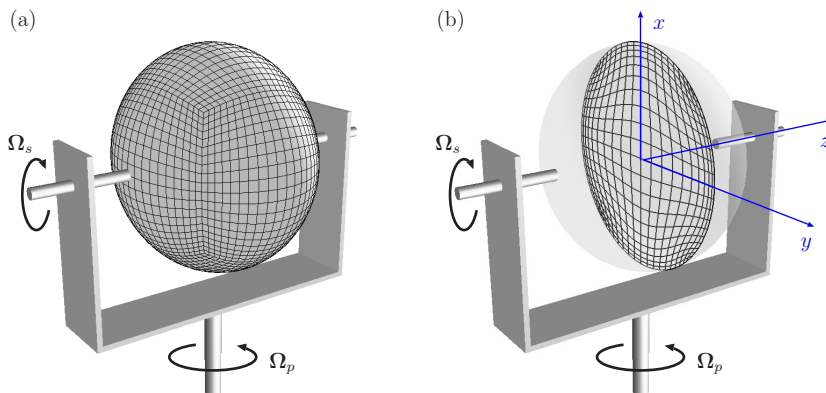


FIG. 1. Processing spheroid with the spin and precession axes being at a right angle. Numerical grid is shown on (a) the cavity wall and (b) the equatorial plane. For visibility, the number of the grid points is reduced. The coordinates  $(x, y, z)$  fixed on the rotating frame (the precession frame) are defined so that the spin and precession axes are parallel to the  $z$  and  $x$  axes, respectively.

In fact, many studies have been conducted to understand the flow in precessing containers. The modern theoretical studies go back to the one by Poincaré [1], and important contributions have been continuously made [2–4] for steady flow and its instability in the weak precession regime. However, since it is difficult to establish a nonlinear theory applicable to the turbulence regime, laboratory experiments, which were first conducted by Malkus [5] and Vanyo and Linkins [6], have been leading this research field. Even by using state-of-art techniques, however, the information on the flow obtained in the laboratory is limited. In particular, it is difficult to measure three-dimensional flow fields in a precessing container.

Direct numerical simulations (DNSs) therefore must play a crucial role. Tilgner [7–9] conducted the first DNSs of flow in precessing spherical and spheroidal shells, and later quite a few DNSs of precession-driven flow were conducted not only by himself and his coworkers [10–13] but also by many other researchers (see the recent DNS studies [14–24] and references therein). It is only recently, however, that we can conduct the DNS of turbulent flow in a precessing full sphere under conditions similar to the laboratory experiments [25,26]. These DNSs [25,26] for the precessing sphere employed the spectral method in terms of the spherical harmonics and Jacobi polynomials. Although we may use a coordinate transformation to conduct the DNS of flow in a spheroid or a spheroidal shell [10], it is not necessarily effective to extend the spectral method to the DNS of flow in a spheroid, because of the coordinate singularity and the grid-point concentration along the symmetry axis of the spherical coordinate. Therefore, Chan *et al.* [14] and Zhang *et al.* [17] employed a finite element method in the DNS of precession-driven flow in an oblate spheroid. To our knowledge, Refs. [14,17] were the first DNSs of precession-driven flow in spheroids, but no DNS has been conducted to focus on developed turbulence, which is the target of the present study, in precessing spheroids. In the present study, we conduct DNSs by using a finite difference method, instead of the spectral or finite element methods, adopting an appropriate grid generation algorithm so that we also avoid the above mentioned difficulties of the spherical coordinate. Since the generated grid is boundary-fitted, the boundary condition is accurately imposed. In addition, to efficiently conduct the DNSs, we make the numerical grid finer only in near-wall regions. In addition, the parallel computing is also straightforward compared to the spectral methods. A disadvantage is in the complexity of the coding due to the adoption of the curvilinear coordinate. Nevertheless, it is advantageous that we can easily change the shape of the container. We conduct, making use of this advantage, a series of DNSs of turbulent flows in precessing spheroids with different values of the ellipticity.

In the present paper, we show DNS results for the ellipticity dependence of flow in spheroids. It was shown by the theory on inviscid flow by Poincaré [1], by the theory on viscous flow by Busse [2], and by the laboratory experiments by Malkus [5] that a small ellipticity significantly affects the flow states. Our DNSs, of course, realize this feature of the significant dependence of flow states on the ellipticity of the container. Furthermore, our DNSs show the accurate route to turbulence as well as the detailed three-dimensional turbulent flow structures in the precessing spheroids.

## II. DIRECT NUMERICAL SIMULATIONS

### A. Governing equations

We investigate flow of a confined fluid in precessing spheroids. As depicted in Fig. 1, a container with a spheroidal cavity spins at a constant angular velocity  $\boldsymbol{\Omega}_s$  and the spin axis rotates about another axis (the precession axis) at a constant angular velocity  $\boldsymbol{\Omega}_p$ . In our setup, we restrict ourselves in the case that the spin axis is perpendicular both to the equatorial plane of the spheroid and to the precession axis. We observe the flow in the noninertial frame (the precession frame), which rotates at  $\boldsymbol{\Omega}_p$  with respect to the laboratory. The Cartesian coordinates  $(x, y, z)$  are fixed in the precession frame and defined as shown in Fig. 1, namely, the  $x$  and  $z$  axes are parallel to the precession and spin axes, respectively.

We numerically simulate the flow of an incompressible Newtonian fluid (with constant mass density  $\rho$  and kinematic viscosity  $\nu$ ) confined in the spheroid. By using the reciprocal  $\Omega_s^{-1}$  of the spin angular velocity, the equatorial radius  $a$  of the cavity, and  $a^3\rho$  as the characteristic time, length, and mass, respectively, we nondimensionalize the Navier-Stokes equation in the precession frame to obtain

$$\frac{\partial \mathbf{u}}{\partial t} + \mathbf{u} \cdot \nabla \mathbf{u} = -\nabla p + \frac{1}{\text{Re}} \nabla^2 \mathbf{u} + 2\text{Po} \mathbf{u} \times \widehat{\mathbf{e}}_p. \quad (1)$$

Here  $\mathbf{u}(\mathbf{x}, t)$ ,  $p(\mathbf{x}, t)$ ,  $\mathbf{x}$ , and  $t$  are the nondimensionalized fluid velocity, pressure, position vector, and time, respectively. The nondimensionalized equation of continuity and boundary condition on the cavity wall are expressed by

$$\nabla \cdot \mathbf{u} = 0 \quad (2)$$

and

$$\mathbf{u} = \widehat{\mathbf{e}}_s \times \mathbf{x} \quad \text{on} \quad x^2 + y^2 + \left( \frac{z}{1-\eta} \right)^2 = 1. \quad (3)$$

In Eqs. (1) and (3),  $\widehat{\mathbf{e}}_s$  and  $\widehat{\mathbf{e}}_p$  denote the unit vectors parallel to the spin and precession axes, respectively. The governing equations (1)–(3) depend on three nondimensional parameters, i.e., the Reynolds number (the spin rate),

$$\text{Re} = \frac{a^2 \Omega_s}{\nu}, \quad (4)$$

the Poincaré number (the precession rate),

$$\text{Po} = \frac{\Omega_p}{\Omega_s}, \quad (5)$$

and the ellipticity of the cavity,

$$\eta = \frac{a-b}{a}, \quad (6)$$

with  $b$  being the polar radius. Flow in the precessing spheroid (Fig. 1) is therefore controlled by these three parameters (Re, Po,  $\eta$ ).

## B. Numerical schemes

We briefly summarize the numerical scheme of our DNSs. We use a standard finite difference scheme, but we do not solve the governing equations in the spherical coordinate, which is usually employed for the DNS of flow in a full sphere, a spherical, or spheroidal shell because one can easily impose the boundary condition (3) on the cavity wall. As mentioned in Sec. I, the disadvantages of DNS in the spherical coordinate are the following. First, we need special treatments to evaluate the spatial derivatives due to the coordinate singularities. Second, and more seriously, the grid points concentrate along the symmetry axis, where the velocity derivatives are not necessarily large. We therefore use a boundary-fitted coordinate, shown in Fig. 1, so that we can avoid these difficulties of the spherical coordinate. More concretely, we first generate the cubed sphere grid [27] on the container's wall, which is used for the boundary condition of the Poisson equation to generate a grid inside the container. By putting appropriate source terms in the Poisson equation, we can make the grid finer in near-wall regions. See Appendix A for the details of the grid generation algorithm.

We emphasize that the construction method of the boundary-fitted grid is flexible and applicable to containers other than a sphere. In the present DNS, in fact, we can easily conduct DNSs of flow in a sphere, a spheroid, a cylinder, and even a channel without changing the main code. This advantage enables us to conduct the DNS of flow in precessing spheroids with different values of the ellipticity (6). We then investigate the ellipticity dependence of the flow transitions on turbulence and the three-dimensional flow structures and statistics of the sustained turbulence.

Apart from the grid, our numerical schemes are standard. We use a second-order finite difference method with the collocate grid in the curvilinear coordinate [28], where we assign the three velocity components in the Cartesian coordinate and the pressure at the center of each grid cell, whereas we assign the mass flux on the side of each cell. These assignments of the variables ensure the mass conservation. For the temporal integration, we use the second-order Crank-Nicolson method for the viscous term and the second-order Adams-Bashforth method for the other terms in Eq. (1). The SMAC method is employed for the coupling of (1) and (2), and the Poisson equation for the pressure is solved iteratively using the SOR method.

## C. Validation

To validate the DNS results, we compare them with experimental data in Fig. 2. As described in detail in Refs. [29,30], we can measure the velocity field only on the equatorial plane of the containers in our experiments using particle image velocimetry. We therefore compare the temporally averaged velocity field on the plane for two different containers with  $\eta = 0$  and 0.1. The temporal average is taken over 50 spin periods both in the experiments and in the DNSs. Figures 2(a) and 2(b) and Figs. 2(c) and 2(d) show the cases with the spherical and spheroidal cavities, respectively. The parameters are common:  $\text{Re} = 10^4$  and  $\text{Po} = 0.1$ . The numerical results are in good agreement with the experimental data.

Incidentally, we have confirmed that, for this Reynolds number ( $\text{Re} = 10^4$ ), when we use grid points less than  $98^3$ , the results are inconsistent with experimental data, although the DNS is stably conducted. The convergence tolerance of the correction pressure  $\phi$  also affects the results. We therefore impose the condition

$$\frac{\|\phi^{(m+1)} - \phi^{(m)}\|}{\|\phi^{(m)}\|} < 10^{-3}, \quad (7)$$

where  $\|\cdot\|$  is the  $L_2$ -norm and  $m$  denotes the number of the iteration, to judge the convergence. The results shown below are by the DNSs with  $98^3$  grid points and the convergence tolerance (7) for the Poisson equation.

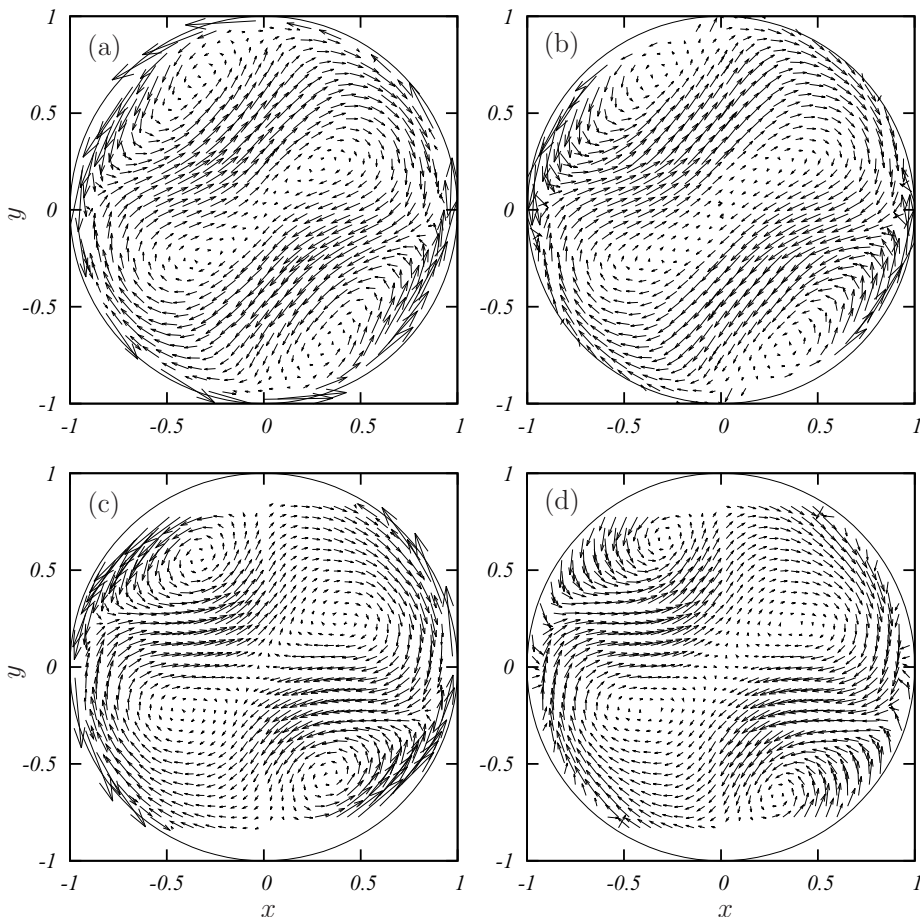


FIG. 2. Comparison of the temporally averaged (over 50 spin periods) velocity field on the equatorial plane of (a), (b) the precessing sphere and (c), (d) spheroid with  $\eta = 0.1$ . Results of (a), (c) the DNSs with the number of grid points being  $98^3$  and (b), (d) laboratory experiments. Parameters are common:  $\text{Re} = 10^4$  and  $\text{Po} = 0.1$ . The length of the vectors is normalized so that  $a\Omega_s$  becomes unity. The DNS results are plotted, by interpolation, only on the points where the experimental data exist.

### III. RESULTS

The most interesting feature of the flow in a precessing container is that relatively weak precession of the container leads to developed turbulence. It is therefore crucial to reveal (1) the condition that turbulence is sustained and (2) the detailed three-dimensional structures of sustained turbulence. As will be shown in this section, the present DNSs may reveal these.

#### A. Sustainability condition of developed turbulence

When we increase  $\text{Po}$  from 0, for a fixed value of  $\text{Re}$ , flow in a precessing spheroid changes as the solid-body rotational ( $\text{Po} = 0$ ), steady in the precession frame, periodic, and turbulent flows. It is known, since the experiments by Malkus [5], that the developed turbulence appears suddenly (discontinuously) at a value of  $\text{Po}$ , which is denoted by  $\text{Po}^{(t)}(\text{Re})$ , in a spheroid with sufficiently large ellipticity. In contrast, the flow transition in a precessing sphere is continuous [5,31].

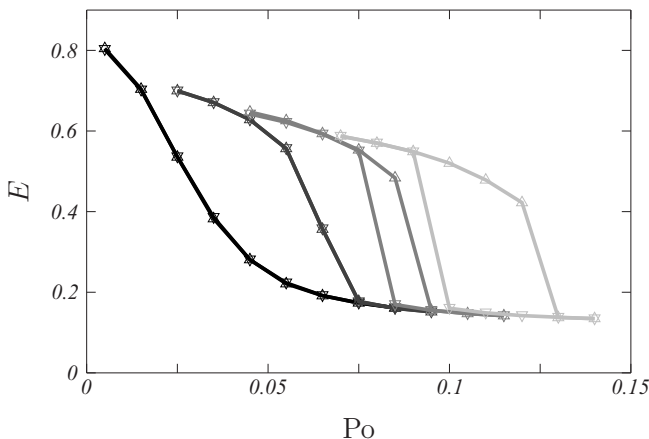


FIG. 3. The temporal average  $E$  of the kinetic energy in the precession frame as a function of  $Po$ . The energy  $E$  attains the maximum for the solid-body rotational flow ( $Po = 0$ ). We examine four different values ( $\eta = 0$ , black curve; 0.1, dark gray; 0.15, gray, 0.2, light gray) of the ellipticity of the spheroidal container. The Reynolds number is fixed at  $Re = 10^4$ . Upper triangles are the results of DNSs with increasing  $Po$ , and lower triangles are those with decreasing  $Po$ . We observe hysteresis loops for  $\eta = 0.15$  and 0.2.

We conduct a series of DNSs with changing the ellipticity of the spheroid in the range that  $0 \leq \eta \leq 0.2$ . For each value of  $\eta$ , we change the value of  $Po$  by step and evaluate the temporal average

$$E = \left\langle \frac{1}{2} \int |\mathbf{u}|^2 d\mathbf{x} \right\rangle \quad (8)$$

of the total kinetic energy in the precession frame for the fixed Reynolds number at  $Re = 10^4$ . We show results in Fig. 3. The value of  $E$  attains the maximum,

$$E_{\max} = \int_{-b/a}^{b/a} \int_0^a \sqrt{1-(az/b)^2} \pi r^3 dr dz = \frac{4\pi(1-\eta)}{15}, \quad (9)$$

which depends on the ellipticity  $\eta$ , for the solid-body rotational flow at  $Po = 0$ , and it decreases as  $Po$  increases.

The upper triangles in Fig. 3 are the results for increasing  $Po$  cases, whereas the lower triangles are those for decreasing  $Po$  cases. This figure clearly shows the qualitative difference of the transition depending on the ellipticity. More concretely, for the examined Reynolds number ( $Re = 10^4$ ), when the ellipticity is larger than about 0.1, the transition is discontinuous and a hysteresis loop exists. In contrast, when  $\eta \lesssim 0.1$ , the transition is continuous, and no hysteresis loop is observed. We will discuss, in Appendix B, the  $Re$  dependence of the minimum  $|\eta|$  for which a discontinuous transition occurs.

As will be shown in detail in the next subsection (Sec. III B), the flow structures for  $Po < Po^{(t)}$  and for  $Po > Po^{(t)}$  are significantly different. For example, when  $\eta = 0.15$ , the former for  $Po < Po^{(t)}$  is in a high-energy (high- $E$ ) state with  $E \approx 0.6$ , which is dominated by a global nearly-uniform-vorticity circulation about an axis inclined from the spin axis due to the Coriolis force [see Fig. 6(b) in Sec. III B]. On the other hand, the latter for  $Po > Po^{(t)}$  is in a low-energy (low- $E$ ) state with  $E \approx 0.15$ , whose mean flow structure is complex [see Fig. 6(c)]. We emphasize that the high- $E$  state has no large-scale shearing motions, and it cannot produce strong turbulence. In other words,  $Po$  must be larger than  $Po^{(t)}$  for sustaining complex large-scale flow and, therefore, developed turbulence. In fact, our laboratory experiments [31] for sufficiently high Reynolds numbers show

that the flow in the low- $E$  state is indeed developed turbulence, in which shearing motions around the twisted mean flow structure produces small-scale turbulent eddies (see Fig. 7 in Sec. III B for the corresponding DNS results).

We observe in Fig. 3 that the transitional Poincaré number  $Po^{(t)}$  is larger for larger  $\eta$ . The container with smaller ellipticity is, therefore, better for the purpose to sustain developed turbulence with smaller  $Po$ . Incidentally, we showed [31] by using the theory by Busse [2] that  $Po^{(t)} \approx |\eta|/2$  for sufficiently high  $Re$ . Although the Reynolds number examined in the present DNSs is not high enough ( $Re = 10^4$ ), the results in Fig. 3 are consistent with the prediction:  $Po^{(t)} \approx |\eta|/2 = 0.1$  for  $\eta = 0.2$ , for example. It may be worth mentioning that, when  $Re$  is sufficiently high,  $Po^{(t)}$  is significantly larger than the critical  $Po$  at which the steady flow becomes unstable due to the inertial-mode resonance (see the experimental results shown in Ref. [31]). We also observe in Fig. 3 that the range of  $Po$  of the hysteresis loop expands as  $\eta$  increases.

In addition, Fig. 3 shows that the  $Po$  dependence of the energy  $E$  above the transition (i.e., in the low- $E$  state for  $Po > Po^{(t)}$ ) is independent of the ellipticity. This result implies that the flow structures in the low- $E$  state only weakly depend on the ellipticity. We will discuss this point in Sec. III D.

### B. Three-dimensional flow structures in the bistable states

We have shown in the preceding subsection (see Fig. 3) that there can be bistable states for a given set of parameters. In this subsection, we compare the three-dimensional flow structures in these states to conclude that they are quite different. More concretely, the low- $E$  state has flow structures that are much more complex than the high- $E$  states, which are the nearly-uniform-vorticity flows. We recall that the energy  $E$  is evaluated in the precession frame, and it takes the maximum (9) for the solid-body rotational flow ( $Po = 0$ ).

We investigate a typical example in detail, i.e., the bistable states at  $Re = 10^4$  and  $Po = 0.085$  in the precessing spheroid with the ellipticity  $\eta = 0.15$ . These two states are both unsteady. We show the temporally averaged velocity fields on cross sections in Fig. 4. The average velocity [Figs. 4(a)–4(c)] in the high- $E$  state is much faster than in the low- $E$  state [Figs. 4(d)–4(f)], and it is as fast as the speed  $a\Omega_s$  of the cavity wall on the equatorial plane. However, the velocity fluctuations are much larger in the low- $E$  state. Evidence is given in Fig. 5, in which the average  $(u'_x + u'_y + u'_z)/3$  of the root mean squares of velocity components is shown. Note the difference in the contour levels in Fig. 5(a) for the high- $E$  state and in Fig. 5(b) for the low- $E$  state. Although the velocity is much faster in the high- $E$  state than in the low- $E$  state (Fig. 4), the velocity fluctuations are significantly larger in the low- $E$  state. We also observe that the high-turbulence-intensity regions are located differently in these two states. The region is annular on the equatorial plane in the high- $E$  states [Fig. 5(a)], which forms a tube in the three-dimensional space [Fig. 5(c)]. On the other hand, the high-turbulence-intensity region in the low- $E$  state is ringlike [Fig. 5(d)]. The origin of the strong turbulence intensity will be discussed below (see Fig. 7).

For this Poincaré number ( $Po = 0.085$ ), the global flow structure in the high- $E$  state is a simple global circulation about an axis which is inclined from the spin axis (the  $z$  axis). Figure 6(b) shows the streamlines of the mean flow in the high- $E$  state. We can see that the principal component of the flow in the high- $E$  state is a simple global circulation.

In contrast to the simple large-scale flow structure [Fig. 6(b)] in the high- $E$  state, the mean flow in the low- $E$  state is nontrivial [Figs. 4(d)–4(f) and 6(c)]. We notice in these figures that the mean flow in a central region of the container is a circulation about the  $y$  axis, which is the axis perpendicular to both the spin and precession axes. However, different from the high- $E$  states [Figs. 4(a)–4(c)], the velocity of this circulation [Figs. 4(d)–4(f)] is much slower than the spin velocity of the cavity wall. We also notice in Fig. 6(c) that the center line of this circulation is twisted, and it cannot be expressed as a uniform-vorticity flow.

It may be interesting to compare the global flow structures with the theory by Busse [2]. As shown in previous studies [11,31–33], the unsteady flow in the high- $E$  state is well approximated

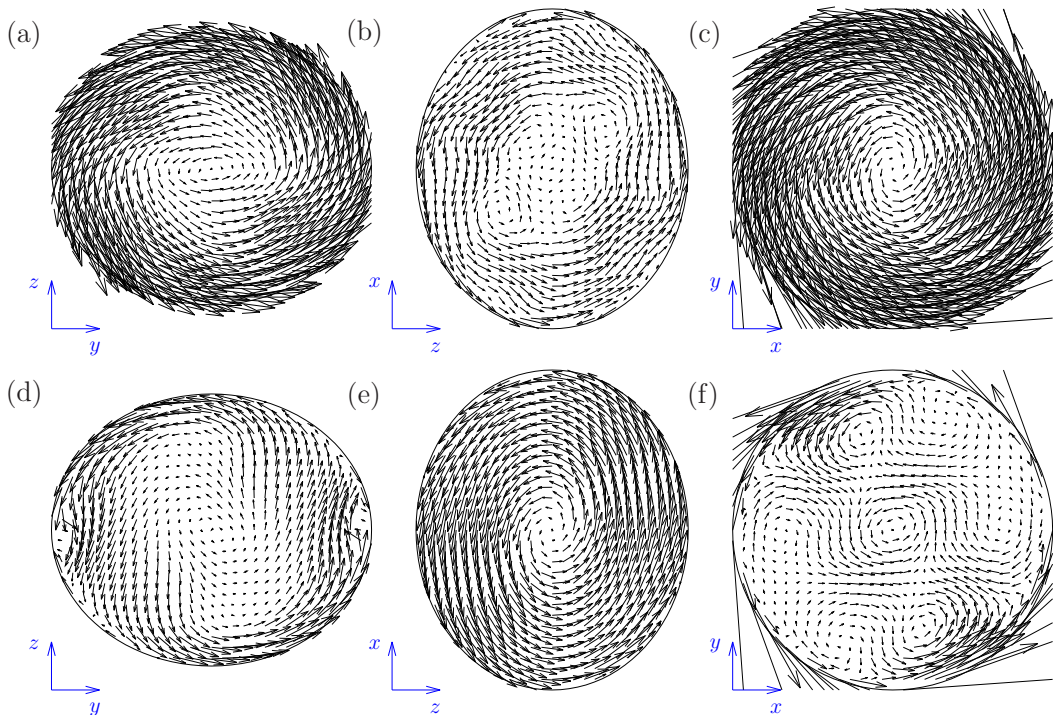


FIG. 4. Temporally averaged velocity fields in the bistable states for  $\text{Re} = 10^4$  and  $\text{Po} = 0.085$  in the precessing spheroid with  $\eta = 0.15$ . We show the mean velocity fields (in the precession frame) on three cross sections of the flow in the (a)–(c) high- $E$  state and (d)–(f) low- $E$  state. It is seen in panel (c) that the fluid velocity in the high- $E$  state is as fast as the velocity  $a\Omega_s$  of the cavity wall on the equatorial plane.

by the steady uniform-vorticity solution [2] derived for low  $\text{Po}$ . To demonstrate this, we plot in Fig. 6 streamlines of the mean flow in a  $\text{Po}$  range around the hysteresis loop and compare them with the steady solution. Figure 6(e) shows the theoretical prediction of the angle  $\varphi$  between the spin axis and the uniform vorticity vector. The vertical lines in Fig. 6(e) indicate the three values of  $\text{Po}$  (0.08, 0.085, and 0.09), for which we show the DNS results in Fig. 6(a), Figs. 6(b) and 6(c), and Fig. 6(d), respectively. Note that the theory predicts that the range of  $\text{Po}$  for the bistable states is  $0.074 \lesssim \text{Po} \lesssim 0.082$ , which is slightly lower than the DNS results. More precisely, we numerically observe the bistable states in a very narrow range around  $\text{Po} = 0.085$  [Figs. 6(b) and 6(c)]. Nevertheless, the steady solutions well approximate the mean flow structures in the hysteresis loop. We can see in Fig. 6(a) that the center line of the mean-flow circulation observed in the high- $E$  state for  $\text{Po} = 0.08$  coincides with the theoretical prediction (the red straight line) of the direction of the vorticity vector. Incidentally, the blue straight lines in Fig. 6 denote the direction of the vorticity of the other steady solution in the low- $E$  states, which correspond to the blue closed circles in Fig. 6(e). It is further interesting to observe, in Figs. 6(c) and 6(d), that the circulation approximately about the  $y$  axis in a central region of the container in the low- $E$  states is also approximated by the steady solution, though, of course, the twisted streamline structures are not expressed by the uniform-vorticity solution. We reemphasize that these are surprising coincidences, since the theory [2] is applicable to steady flows for low  $\text{Po}$  ( $\ll \text{Re}^{-1/2}$ ).

It is further important to observe in Fig. 6(b) that there exist strong shear flows around  $y = \pm a$ , where the internal flow is circulating about the  $y$  axis, whereas the cavity wall and the fluid near the wall rotate about the  $z$  axis. Smaller-scale turbulent eddies are likely to be created by vortex stretching in these shearing regions. To verify this, we show isosurfaces of the enstrophy in Fig. 7.

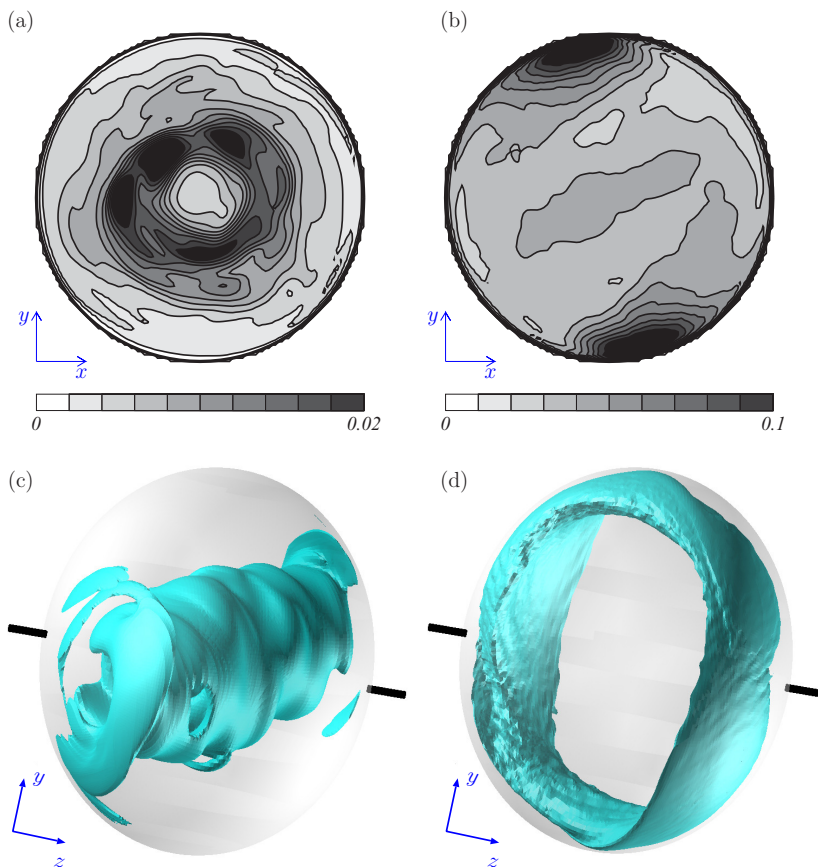


FIG. 5. (a), (b) The contour on the equatorial plane and (c), (d) the isosurface of the average  $(u'_x + u'_y + u'_z)/3$  of root mean squares of three velocity components for  $Re = 10^4$  and  $Po = 0.085$  in the precessing spheroid with  $\eta = 0.15$ . (a), (c) High- $E$  and (b), (d) low- $E$  states. Note the difference in the contour levels in panels (a) and (b). The threshold of the isosurface is (c) 0.014 and (d) 0.07.

In the low- $E$  state [Fig. 7(b)], strong small-scale turbulent eddies are indeed created in these regions and circulating along the mean-flow streamlines. Incidentally, this ringlike region with turbulent eddies was observed in a precession-driven turbulence in a sphere [34]. On the other hand, since the mean flow in the high- $E$  state is not accompanied by a shearing motion, no small-scale eddies are observed in Fig. 7(a). Instead, we observe cavity-size ringlike vortical structures in the high- $E$  state. We note that the threshold of the enstrophy isosurface in Fig. 7(b) is 4.8 times larger than in Fig. 7(a). This means that much stronger smaller-scale vortices exist in the low- $E$  states than the high- $E$  states. It is this difference in the intensity of smaller-scale vortices in the high- and low- $E$  states that explains the difference of the magnitude of velocity fluctuations shown in Fig. 5. In fact, the ringlike region with high turbulence intensity [Fig. 5(d)] coincides with the region with small-scale vortices [Fig. 7(b)].

In summary, large-scale flows in the bistable states are essentially different from each other (Fig. 6). The shearing regions ( $y \approx \pm a$ ) in the nontrivial large-scale flow in the low- $E$  state play an important role for sustaining small-scale turbulent eddies [Fig. 7(b)]. In fact, for higher  $Re$ , fully developed turbulence is sustained by the large-scale structures in the low- $E$  state [30]. Experiments for higher  $Re$  also showed that flows in the high- $E$  states were quiescent turbulence, whereas those in the low- $E$  states were fully developed (see the visualizations in Fig. 3 of Ref. [31]).

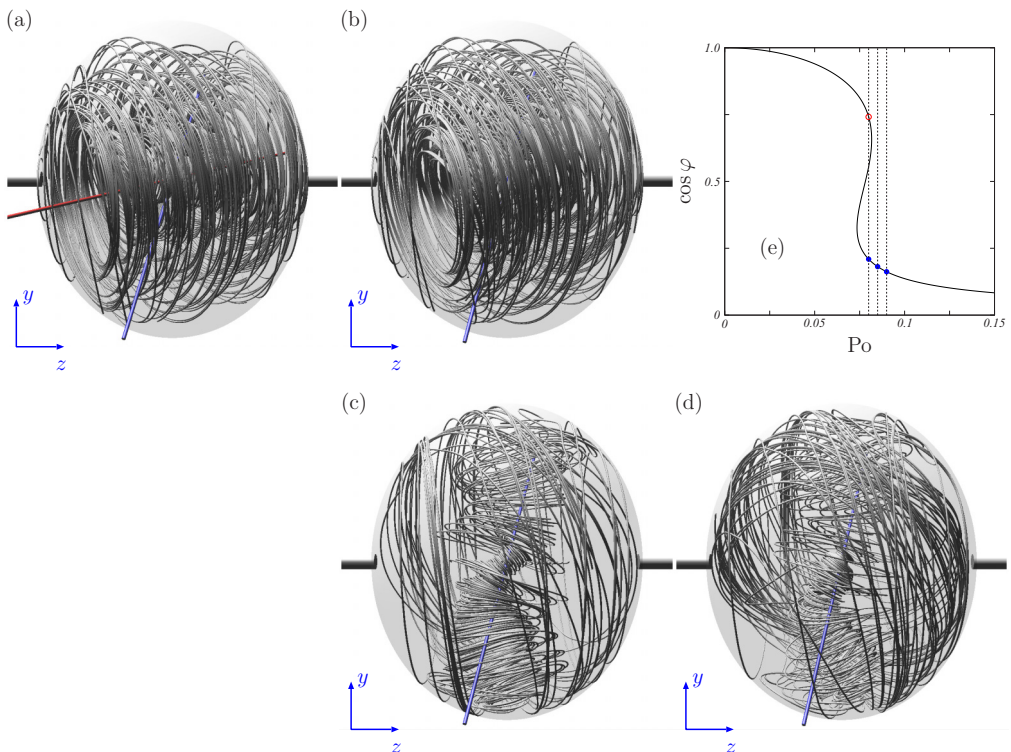


FIG. 6. Three-dimensional flow structures in a  $Po$  range around the hysteresis loop for  $Re = 10^4$  and  $\eta = 0.15$ . The Poincaré number is (a)  $Po = 0.08$ , (b), (c)  $0.085$ , and (d)  $0.09$ . For  $Po = 0.08$  and  $0.09$ , we observe only flows in the (a) high- and (d) low- $E$  states, respectively. The precession with  $Po = 0.085$  sustains bistable states with (b) high and (c) low energy. Panel (e) shows the theoretical prediction [2] of the angle  $\varphi$  between the spin ( $z$ ) axis and the vorticity vector of the steady uniform-vorticity flow. The dotted vertical lines in panel (e) indicate the three values ( $0.08$ ,  $0.085$ , and  $0.09$ ) of  $Po$ . The red and blue straight lines in panels (a)–(d) indicate the direction of the uniform vorticity vector of the steady flow in the high- and low- $E$  states, respectively.

### C. Laminarization for higher $Po$

For further higher  $Po$ , the turbulent flow in a precessing cavity laminarizes in a central region of the container. This interesting phenomenon has not been emphasized, but it is important. We show the evidence of the laminarization in Fig. 8, where we draw streamlines of the temporally averaged velocity field for six values of  $Po$  between  $0.2$  and  $2$ . The Reynolds number and the ellipticity are fixed at  $Re = 10^4$  and  $\eta = 0.15$ , respectively. The line of sight is parallel to the  $x$  (precession) axis, and only streamlines in a hemisphere ( $x > 0$ ) are drawn.

The observed mean-flow structures are interesting. For the examined condition ( $Re = 10^4$  and  $\eta = 0.15$ ), the mean-flow streamlines for  $Po \lesssim 0.3$  are complex [see Figs. 8(a) and 8(b) for  $Po = 0.2$  and  $0.3$ ; see also Fig. 6(b) for  $Po = 0.085$ ]. In contrast, for  $Po$  larger than  $0.4$  [Fig. 8(c)], the turbulence in a central region is significantly reduced. More concretely, flow becomes a simple two-dimensional circulation about the precession ( $x$ ) axis in the central region of the container. This two-dimensionalization occurs only in the central region, and turbulence is still sustained but confined in an outer region. We observed this laminarization in laboratory experiments [29], but the present DNS first reveals its three-dimensional structures. Recall that we observe the flow in the precession frame. The circulation in the central region implies that the fluid rotates in a different (in

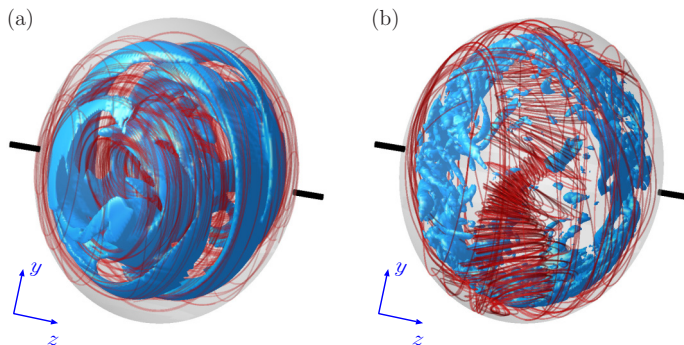


FIG. 7. Isosurfaces (blue objects) of the instantaneous enstrophy field in the (a) high- $E$  state and (b) low- $E$  state. The threshold is set to be (a)  $2.5\Omega_s^2$  and (b)  $12\Omega_s^2$ . Structures in the boundary layer near the wall ( $\sqrt{x^2 + y^2 + [z/(1-\eta)]^2} > 0.9a$ ) are not shown. Red curves are the streamlines shown in Fig. 6.

fact, faster) angular velocity from  $\Omega_p$  in the laboratory frame. The contrast between turbulent and laminar regions gets clearer for higher Po [Figs. 8(e) and 8(f)].

This laminarization for relatively high Po, which is actually lower than 1, stems from the fact that the precession axis is fixed in the laboratory frame. In other words, this is a well-known phenomenon in rotating systems. Therefore, even if we change the container's shape, it is difficult to avoid the laminarization in a high Po range. We reemphasize that the laminarization occurs for Po which is

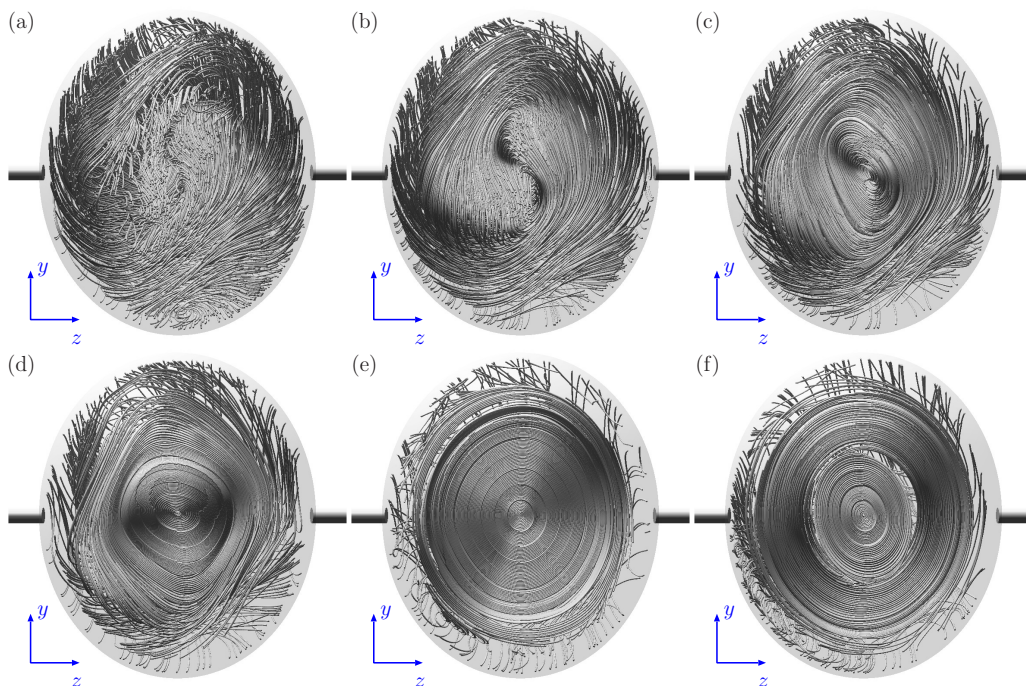


FIG. 8. Laminarization in a central region along the precession axis for higher Po. We draw streamlines of the temporally averaged field in a hemisphere ( $x > 0$ ). The Reynolds number is fixed at  $\text{Re} = 10^4$ , and the Poincaré number is changed as (a)  $\text{Po} = 0.2$ , (b)  $0.3$ , (c)  $0.4$ , (d)  $0.5$ , (e)  $1$ , and (f)  $2$ . The ellipticity of the cavity is  $\eta = 0.15$ .

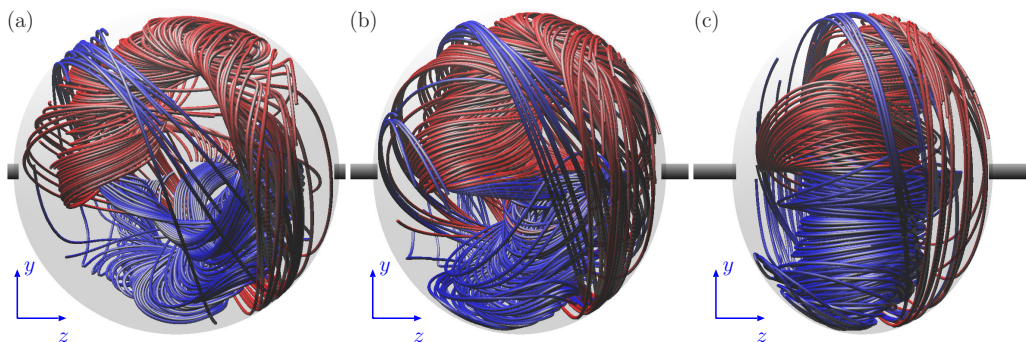


FIG. 9. Streamlines of mean flow in the spheroids with different ellipticity: (a)  $\eta = 0$ , (b) 0.1, and (c) 0.2. Flow parameters are common:  $Po = 0.1$  and  $Re = 10^4$ . Streamlines are drawn from the spin axis, and colored in red for those towards  $y > 0$  and in blue for those towards  $y < 0$ . Red (or blue) streamlines are right-hand (or left-hand) spirals.

not that high (say,  $Po \gtrsim 0.4$  for  $Re = 10^4$  as shown in Fig. 8). This is important information for the sustainability condition of strong turbulence in precessing containers.

#### D. Ellipticity dependence of the low-energy states

Another interesting observation in Fig. 3 is that the different curves for different values of  $\eta$  coincide for  $Po > Po^{(t)}$ , namely, the energy  $E$  of the low-energy states is independent of  $\eta$ . This implies that the flow in these states is only weakly dependent on the ellipticity. We show in Fig. 9 streamlines of mean flow in the spheroids with ellipticity  $\eta = 0, 0.1$ , and  $0.2$ . The flow parameters are common:  $Re = 10^4$  and  $Po = 0.1$ . Streamlines are drawn from the points on the spin axis (i.e., the  $z$  axis). The streamline topology is, indeed, common in these containers irrespective of the ellipticity. It is also similar to the one shown in Fig. 6(b) for  $\eta = 0.15$  and  $Po = 0.85$ . In this intermediate  $Po$  range ( $Po \approx 0.1$ ), the flow is dominated by circulations about the  $y$  axis, which is the axis perpendicular to both the spin and precession axes. In particular, for the largest ellipticity examined [ $\eta = 0.2$ , Fig. 9(c)], the mean flow seems a relatively simple circulation about the  $y$  axis. However, the streamlines are actually spirals, and the fluid slowly flows towards  $y = \pm a$ . The red (or blue) curves towards the  $y > 0$  (or  $y < 0$ ) hemisphere are right-hand (or left-hand) spirals. For smaller  $\eta$ , these spirals are curved, and they form a pair of banana-shaped vortices in the sphere [ $\eta = 0$ , Fig. 9(a)]. As shown in Sec. III B (Fig. 7), the shear flow around these large-scale vortices plays important roles in producing small-scale turbulent eddies. We also showed in Ref. [25] that the pair of the banana-shaped vortices sustains strong mixing in the precessing sphere.

For comparison, we also conduct the DNS of turbulence in prolate spheroids with the ellipticity being  $-0.1$  and  $-0.2$ . By setting appropriate initial conditions, we realize turbulence in the low- $E$  state for the common set of the flow parameters ( $Po = 0.1$  and  $Re = 10^4$ ). Figures 10(b) and 10(c) show the streamlines of the mean velocity field of the simulated turbulence in the prolate spheroids, and Fig. 10(a) shows the streamlines in the sphere [Fig. 9(a)] from the same viewpoint as in Fig. 10(b). Comparing Fig. 10(a) for  $\eta = 0$  with Fig. 10(b) for  $\eta = -0.1$ , we can see that the mean flow structures in these cavities are similar. In particular, the pair of twisted vortices exists in the both cavities. Although similar twisted vortices are observed in the prolate spheroid with a larger, in magnitude, ellipticity [ $\eta = -0.2$ , Fig. 10(c)], their orientation is different from those observed in Figs. 10(a) and 10(b). Note that we rotate the objects with the angle  $\pi/4$  about the  $z$  axis in Fig. 10(c) with respect to Figs. 10(a) and 10(b). It is important that the twisted (banana-shaped) vortices exist in these prolate spheroids because they effectively generate small-scale turbulent eddies in the shear flows around them. Therefore, if the Reynolds number is high enough, these spheroids may also

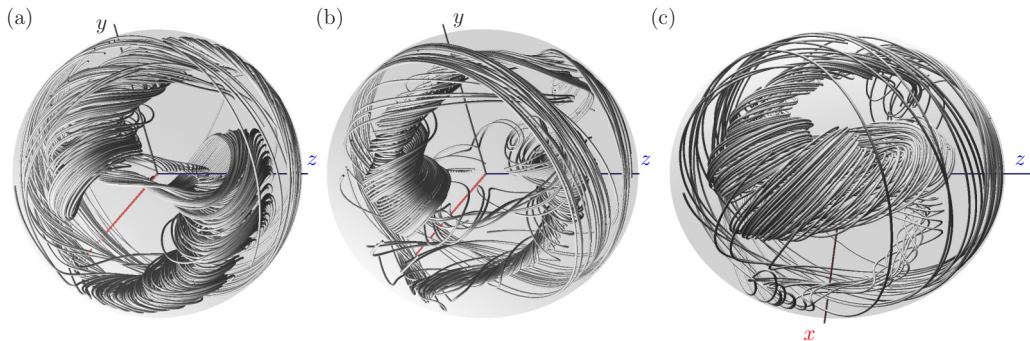


FIG. 10. Streamlines of mean flow in (a) the precessing sphere and prolate spheroids with the ellipticity (b)  $\eta = -0.1$  and (c)  $-0.2$ . Flow parameters are common:  $Po = 0.1$  and  $Re = 10^4$ . Panel (a) shows the same streamlines as in Fig. 9(a) but from a different viewpoint. Note that we rotate the objects so that we can see the twisted vortices; the line of sight in panel (c) is different with the angle  $\pi/4$  (around the  $z$  axis) from panels (a) and (b).

sustain fully developed turbulence. However, recalling the laminar-turbulent transition shown in Fig. 3, the low- $E$  state, for  $Po \approx 0.1$ , cannot be sustained in spheroids with larger  $|\eta|$ . Therefore, the weak precession ( $Po \approx 0.1$ ) sustains strong turbulence if and only if  $|\eta| \lesssim 0.2$ .

#### IV. CONCLUSIONS

We have conducted the DNSs of turbulence in precessing spheroids. The simulated velocity fields are in good agreement with the experimental data (Fig. 2). In particular, we numerically realize bistable flow states for a given set of parameters ( $Re$ ,  $Po$ ) and hysteresis loops connecting them (Fig. 3). (See Appendix B for the condition under which a hysteresis loop appears.) Systematically changing the Poincaré number  $Po$  and the ellipticity  $\eta$  of the cavity for a fixed  $Re (=10^4)$ , we have revealed the condition for developed turbulence to be sustained in precessing spheroids and the three-dimensional flow structures of the sustained turbulence.

For the sustainability condition of developed turbulence in precessing spheroids, we have to consider two facts. One is that the developed turbulence is sustained only in the low- $E$  state (Fig. 7). The low- $E$  states are realized when  $Po \gtrsim 0.1$  in a sphere and spheroids with small ellipticity, whereas it is sustained when  $Po > Po^{(t)} \approx |\eta|/2$  for larger  $|\eta|$  (Sec. III A). Therefore, for larger  $|\eta|$ , the developed turbulence requires higher  $Po$  (Fig. 3). The other is the fact that the turbulence is drastically reduced in a central region when  $Po$  is large (Fig. 8). This laminarization in a central region, which is a well-known phenomenon in rotating systems, occurs for  $Po \gtrsim 0.2$  [29], and it is significant for  $Po \gtrsim 0.4$  [Fig. 8(c)]. Hence, in order to simultaneously satisfy these two conditions to sustain developed turbulence, we should use a spheroidal cavity with small ellipticity.

Although the ellipticity significantly affects the sustainability condition of the low- $E$  state and therefore of the developed turbulence, the energy  $E$  in the low- $E$  states is only weakly dependent on  $\eta$  (Fig. 3). We also observe that the three-dimensional flow structures in the low- $E$  states have common features irrespective of  $\eta$  (Figs. 9 and 10). The observed large-scale flow structures explain the physical mechanism to sustain developed turbulence in the low- $E$  states; namely, there exist strong shear flows between the internal large-scale flow, which is dominated by the circulation about the  $y$  axis (Figs. 9 and 10), and the near-wall circulation about the spin ( $z$ ) axis. It is in this shear flows that small-scale turbulent eddies are amplified [Fig. 7(b)]. Furthermore, when the ellipticity is small (say,  $|\eta| \lesssim 0.1$ ), the large-scale vortices are twisted in a nontrivial manner [Figs. 9(a), 9(b), 10(a), and 10(b)], and there exist internal shear layers. Therefore, when the Reynolds number is high enough, small-scale turbulent eddies are effectively generated in these cavities. Such well-developed turbulent flow in a spheroid with a small ellipticity seems

plausible for effective mixing of the confined fluid as well as for the precession-driven dynamo. For larger  $|\eta|$ , the internal large-scale flow is relatively simple. It is a simple circulation about the  $y$  axis for  $\eta = 0.2$  [Fig. 9(c)], whereas it seems to tend to the circulation about the spin ( $z$ ) axis for  $\eta = -0.2$  [Fig. 10(c)]. For further larger  $|\eta|$  ( $\gtrsim 0.2$ ), as repeatedly discussed above (see Sec. III A), no low- $E$  states, and therefore no developed turbulence, are sustained by weak precession ( $Po \approx 0.1$ ).

The study of the flow in a precessing spheroid has a long history. The year of the submission of the present paper is the 50th anniversary of the two important studies: the seminal laboratory experiment by Malkus [5], which showed that turbulence could be sustained in precessing containers, and the excellent theory of Busse [2], which derived steady flow solutions of the viscous fluid confined in precessing spheroids. It was shown in Refs. [11,31–33] that the theory of Busse for steady flows can explain the hysteresis loop discovered in the experiments by Malkus. Although it took a half century to reveal the detailed three-dimensional turbulent flow structures in precessing spheroids, since adequate numerical environments for the study of precession-driven turbulence are now available, we expect significant progress of our understanding of this fascinating flow system in a few years.

### ACKNOWLEDGMENTS

This study was partly supported by JSPS Grant-in-Aid for Scientific Research (16H04268). Some of the DNSs were conducted under the auspices of the NIFS Collaboration Research Program (NIFS17KNSS101).

### APPENDIX A: GRID GENERATION ALGORITHM

In this Appendix, we describe the generation method of the grid used in our DNS of flow in a sphere. The grids in spheroids are constructed by the linear transformation of the grid in the sphere. First, we generate a grid on the spherical surface by using the method proposed by Ronchi *et al.* [27]. We set the circumscribed cube with the sphere and project grids on the six sides of the cube onto the spherical surface. Next, we generate a grid inside the sphere. Our goal is to construct curvilinear coordinates  $(\xi, \eta, \zeta)$ . For this purpose, we solve the Poisson equations,

$$\xi_{xx} + \xi_{yy} + \xi_{zz} = P(\xi, \eta, \zeta), \quad (\text{A1})$$

$$\eta_{xx} + \eta_{yy} + \eta_{zz} = Q(\xi, \eta, \zeta), \quad (\text{A2})$$

$$\zeta_{xx} + \zeta_{yy} + \zeta_{zz} = R(\xi, \eta, \zeta), \quad (\text{A3})$$

where the subscripts denote the spatial derivatives. We interpret  $\xi$  and  $P$  in Eq. (A1) as the *temperate* and *heat source*. Then we impose the boundary condition of the temperature on the spherical boundary by the value obtained in the first step. Since the solution to (A1) is the steady solution of the heat equation, the isothermal surfaces (i.e., the constant  $\xi$  surfaces) give smooth surfaces which satisfy the boundary conditions. Similarly, the solutions to (A2) and (A3) give smooth spatial distributions of  $\eta$  and  $\zeta$ . In practice, however, we do not solve (A1)–(A3) because we need  $(x, y, z)$  as functions of  $(\xi, \eta, \zeta)$ . Instead, we solve the equivalent equations [35],

$$\alpha_{11}x_{\xi\xi} + \alpha_{22}x_{\eta\eta} + \alpha_{33}x_{\zeta\zeta} + 2(\alpha_{12}x_{\xi\eta} + \alpha_{13}x_{\xi\zeta} + \alpha_{23}x_{\eta\zeta}) = -J^2(Px_{\xi} + Qx_{\eta} + Rx_{\zeta}), \quad (\text{A4})$$

$$\alpha_{11}y_{\xi\xi} + \alpha_{22}y_{\eta\eta} + \alpha_{33}y_{\zeta\zeta} + 2(\alpha_{12}y_{\xi\eta} + \alpha_{13}y_{\xi\zeta} + \alpha_{23}y_{\eta\zeta}) = -J^2(Py_{\xi} + Qy_{\eta} + Ry_{\zeta}), \quad (\text{A5})$$

$$\alpha_{11}z_{\xi\xi} + \alpha_{22}z_{\eta\eta} + \alpha_{33}z_{\zeta\zeta} + 2(\alpha_{12}z_{\xi\eta} + \alpha_{13}z_{\xi\zeta} + \alpha_{23}z_{\eta\zeta}) = -J^2(Pz_{\xi} + Qz_{\eta} + Rz_{\zeta}), \quad (\text{A6})$$

which are obtained by interchanging the independent and dependent variables of (A1)–(A3). Here  $\alpha_{jk}$  and  $J$  are given by

$$\begin{aligned}
 \alpha_{11} &= J^2(\xi_x^2 + \xi_y^2 + \xi_z^2) \\
 \alpha_{22} &= J^2(\eta_x^2 + \eta_y^2 + \eta_z^2) \\
 \alpha_{33} &= J^2(\zeta_x^2 + \zeta_y^2 + \zeta_z^2) \\
 \alpha_{12} &= J^2(\xi_x\eta_x + \xi_y\eta_y + \xi_z\eta_z) \\
 \alpha_{13} &= J^2(\xi_x\zeta_x + \xi_y\zeta_y + \xi_z\zeta_z) \\
 \alpha_{23} &= J^2(\eta_x\zeta_x + \eta_y\zeta_y + \eta_z\zeta_z)
 \end{aligned} \tag{A7}$$

and

$$J = x_\xi y_\eta z_\zeta + x_\eta y_\zeta z_\xi + x_\zeta y_\xi z_\eta - x_\xi y_\zeta z_\eta - x_\eta y_\xi z_\zeta - x_\zeta y_\eta z_\xi, \tag{A8}$$

respectively. We solve (A4)–(A6) by an iterative method, where the derivatives on the right-hand side of (A7) are numerically evaluated by using the formulas such as  $\xi_x = (y_\eta z_\zeta - y_\zeta z_\eta)/J$ .

To attract coordinate surfaces around  $\xi = \Xi$ , we set the source term  $P$  as

$$P(\xi, \eta, \zeta) = -A \operatorname{sgn}(\xi - \Xi) \exp(-C|\xi - \Xi|). \tag{A9}$$

Here  $\operatorname{sgn}(x) = x/|x|$ . By appropriately setting constants  $A$  and  $C$  (we use the values  $A = 8000$  and  $C = 0.4$ ) we can adjust grid width near the wall (i.e.,  $\Xi = 0$  and  $N$  with  $N$  being the number of the grid points in one direction). Similarly, we set the source terms  $Q$  and  $R$  so that we can make the grid finer in a near-wall region in the  $\eta$  and  $\zeta$  directions.

## APPENDIX B: CONDITION FOR A HYSTERESIS LOOP TO EXIST

The steady solutions of Busse [2] approximate unsteady flows in the high- $E$  state. Therefore, the breakdown of the torque balance of the steady flow well describes the subcritical transition from the high- to low- $E$  states [11,31–33]. Using this idea, we derive the condition for the hysteresis loop to appear in the transition between the high- and low- $E$  states. According to the theory,  $Po$  is expressed as a function of the vorticity magnitude  $\omega$ , which is equal to  $\cos \varphi$ , of the sustained steady flow as

$$Po^2 = \left[ \left\{ \frac{0.259}{\sqrt{\operatorname{Re}\omega}} + \eta\omega^2 \right\}^2 + \frac{2.62^2\omega}{\operatorname{Re}} \right] \left( \frac{1}{\omega^2} - 1 \right). \tag{B1}$$

Here we have used  $e_s \perp e_p$ . Note that the ellipticity  $\eta$  appears only in the curly brackets on the right-hand side. If the ellipticity is sufficiently small so that the first term in the curly brackets is dominant, then  $Po$  is a monotonically decreasing function of  $\omega$ . On the other hand, if  $\operatorname{Re}$  is sufficiently high so that the first term is negligible, then  $dPo/d\omega = 0$  for a value of  $\omega$  ( $\in (0, 1)$ ) and therefore the function  $Po(\omega)$  is not monotonic [see an example in Fig. 6(e)]. In such a case, when increasing  $Po$  from 0, we observe a discontinuous behavior of  $\omega$ . The condition for a hysteresis loop to exist is therefore determined by the dominance of the second term in the curly brackets, and it is expressed by

$$\operatorname{Re} > \alpha\eta^{-2}. \tag{B2}$$

Here the coefficient  $\alpha$  is determined by the maximum value of  $\tilde{\alpha}$  such that the function

$$f(\omega) = \left[ \left( \frac{0.259}{\sqrt{\tilde{\alpha}\omega}} + \omega^2 \right)^2 + \frac{2.62^2\omega}{\tilde{\alpha}} \right] \left( \frac{1}{\omega^2} - 1 \right) \tag{B3}$$

of  $\omega$  is a monotonically decreasing function. We estimate  $\alpha = 98.8 \approx 100$ . Hence, for a given  $\text{Re}$ , a hysteresis loop exists for the ellipticity  $|\eta| > 10/\sqrt{\text{Re}}$ . This is consistent with the observation in Fig. 3 that, for  $\text{Re} = 10^4$ , hysteresis loops are observed when  $\eta > 0.1$ .

- 
- [1] H. Poincaré, Sur la précession des corps déformables, *Bull. Astron.* **27**, 321 (1910).
  - [2] F. H. Busse, Steady fluid flow in a precessing spheroidal shell, *J. Fluid Mech.* **33**, 739 (1968).
  - [3] R. R. Kerswell, The instability of precession flow, *Geophys. Astrophys. Fluid Dyn.* **72**, 107 (1993).
  - [4] S. Kida, Steady flow in a rapidly rotating sphere with weak precession, *J. Fluid Mech.* **680**, 150 (2011).
  - [5] W. V. R. Malkus, Precession of the earth as the cause of geomagnetism, *Science* **160**, 259 (1968).
  - [6] J. P. Vanyo and P. W. Linkins, Measurement of energy dissipation in a liquid-filled, precessing, spherical cavity, *J. Appl. Mech.* **38**, 674 (1971).
  - [7] A. Tilgner, Magneto-hydrodynamics flow in precessing spherical shells, *J. Fluid Mech.* **379**, 303 (1999).
  - [8] A. Tilgner, Non-axisymmetric shear layers in precessing fluid ellipsoidal shells, *Geophys. J. Int.* **136**, 629 (1999).
  - [9] A. Tilgner, Spectral methods for the simulation of incompressible flows in spherical shells, *Intl. J. Numer. Mech. Fluids* **30**, 713 (1999).
  - [10] S. Lorenzani and A. Tilgner, Fluid instabilities in precessing spheroidal cavities, *J. Fluid Mech.* **447**, 111 (2001).
  - [11] S. Lorenzani and A. Tilgner, Inertial instabilities of fluid flow in precessing spheroidal shells, *J. Fluid Mech.* **492**, 363 (2003).
  - [12] A. Tilgner, Precession driven dynamos, *Phys. Fluids* **17**, 034104 (2005).
  - [13] A. Tilgner, Kinematic dynamos with precession driven flow in a sphere, *Geophys. Astrophys. Fluid Dyn.* **101**, 1 (2007).
  - [14] K. H. Chan, K. Zhang, and X. Liao, An EBE finite element method for simulating nonlinear flows in rotating spheroidal cavities, *Int. J. Numer. Meth. Fluids* **63**, 395 (2010).
  - [15] C. Nore, J. Léorat, J.-L. Guermond, and F. Luddens, Nonlinear dynamo action in a precessing cylindrical container, *Phys. Rev. E* **84**, 016317 (2011).
  - [16] R. Hollerbach, C. Nore, P. Marti, S. Vantieghem, F. Luddens, and J. Léorat, Parity-breaking flows in precessing spherical containers, *Phys. Rev. E* **87**, 053020 (2013).
  - [17] K. Zhang, K. H. Chan, and X. Liao, On precessing flow in an oblate spheroid of arbitrary eccentricity, *J. Fluid Mech.* **743**, 358 (2014).
  - [18] D. Kong, X. Liao, and K. Zhang, The sidewall-localized mode in a resonant precessing cylinder, *Phys. Fluids* **26**, 051703 (2014).
  - [19] J. Jiang, D. Kong, R. Zhu, and K. Zhang, Precessing cylinders at the second and third resonance: Turbulence controlled by geostrophic flow, *Phys. Rev. E* **92**, 033007 (2015).
  - [20] T. Albrecht, H. M. Blackburn, J. M. Lopez, R. Manasseh, and P. Meunier, Triadic resonances in precessing rapidly rotating cylinder flows, *J. Fluid Mech.* **778**, R1 (2015).
  - [21] A. Giesecke, T. Albrecht, T. Gundrum, J. Herault, and F. Stefani, Triadic resonances in nonlinear simulations of a fluid flow in a precessing cylinder, *New J. Phys.* **17**, 113044 (2015).
  - [22] L. Capanera, J.-L. Guermond, J. Léorat, and C. Nore, Two spinning ways for precession dynamo, *Phys. Rev. E* **93**, 043113 (2016).
  - [23] T. Albrecht, H. M. Blackburn, J. M. Lopez, R. Manasseh, and P. Meunier, On triadic resonance as an instability mechanism in precessing cylinder, *J. Fluid Mech.* **841**, R3 (2018).
  - [24] J. M. Lopez and F. Marques, Rapidly rotating precessing cylinder flows: Forced triadic resonances, *J. Fluid Mech.* **839**, 239 (2018).
  - [25] S. Goto, M. Shimizu, and G. Kawahara, Turbulent mixing in a precessing sphere, *Phys. Fluids* **26**, 115106 (2014).

- [26] Y. Lin, P. Marti, and J. Noir, Shear-driven parametric instability in a precessing sphere, *Phys. Fluids* **27**, 046601 (2015).
- [27] C. Ronchi, R. Iacono, and P. S. Paolucci, The “Cubed Sphere”: A new method for the solution of partial differential equations in spherical geometry, *J. Comput. Phys.* **124**, 93 (1996).
- [28] C. M. Rhie and W. L. Chow, Numerical study of the turbulent flow past an airfoil with trailing edge separation, *AIAA J.* **21**, 1525 (1983).
- [29] S. Goto, A. Matsunaga, M. Fujiwara, M. Nishioka, S. Kida, M. Yamato, and S. Tsuda, Turbulence driven by precession in spherical and slightly elongated spheroidal cavities, *Phys. Fluids* **26**, 055107 (2014).
- [30] Y. Horimoto and S. Goto, Sustaining mechanism of small-scale turbulent eddies in a precessing sphere, *Phys. Rev. Fluids* **2**, 114603 (2017).
- [31] Y. Horimoto, G. Simonet-Davin, A. Katayama, and S. Goto, Impact of a small ellipticity on the sustainability condition of developed turbulence in a precessing spheroid, *Phys. Rev. Fluids* **3**, 044603 (2018).
- [32] J. Noir, P. Cardin, D. Jault, and J.-P. Masson, Experimental evidence of nonlinear resonance effects between retrograde precession and the tilt-over mode within a spheroid, *Geophys. J. Int.* **154**, 407 (2003).
- [33] D. Cébron, Bistable flows in precessing spheroids, *Fluid Dyn. Res.* **47**, 025504 (2015).
- [34] S. Kida and M. Shimizu, A turbulent ring and dynamo in a precessing sphere, *J. Phys.: Conf. Ser.* **318**, 072031 (2011).
- [35] J. F. Thompson, Z. U. A. Warsi, and C. W. Mastin, Boundary-fitted coordinate systems for numerical solution of partial differential equations—A review, *J. Comput. Phys.* **47**, 1 (1982).